

The Megamaser Cosmology Project: IV. A Direct Measurement of the Hubble Constant from UGC 3789

M. J. Reid¹, J. A. Braatz², J. J. Condon², K. Y. Lo², C. Y. Kuo², C. M. V. Impellizzeri² & C. Henkel³

ABSTRACT

In Papers I and II from the Megamaser Cosmology Project (MCP), we reported initial observations of H₂O masers in an accretion disk of a supermassive black hole at the center of the galaxy UGC 3789, which gave an angular-diameter distance to the galaxy and an estimate of H_0 with 16% uncertainty. We have since conducted more VLBI observations of the spatial-velocity structure of these H₂O masers, as well as continued monitoring of its spectrum to better measure maser accelerations. These more extensive observations, combined with improved modeling of the masers in the accretion disk of the central supermassive black hole, confirm our previous results, but with significantly improved accuracy. We find $H_0 = 71.6 \pm 5.7 \text{ km s}^{-1} \text{ Mpc}^{-1}$; this estimate of H_0 is independent of other methods and is accurate to $\pm 8\%$, including sources of systematic error. This places UGC 3789 at a distance of 47.6 Mpc, with a central supermassive black hole of $1.11 \times 10^7 M_\odot$.

Subject headings: Hubble Constant — Cosmology — Dark Energy — General Relativity — distances — individual sources (UGC 3789)

1. Introduction

Measurements of the expansion history of the universe, $H(z)$, play a fundamental role in our understanding of cosmological evolution and its far-reaching physical implications,

¹Harvard-Smithsonian Center for Astrophysics, 60 Garden Street, Cambridge, MA 02138, USA

²National Radio Astronomy Observatory, 520 Edgemont Road, Charlottesville, VA 22903

³Max-Planck-Institut für Radioastronomie, Auf dem Hügel 69, 53121 Bonn, Germany

including addressing the nature of dark energy, the curvature of space, the masses of neutrinos, and the number of families of relativistic particles. While detailed measurements of the cosmic microwave background (CMB, e.g. Komatsu et al. (2011)) allow us to measure linear scales at redshift $z \approx 1100$, this only provides information at a single epoch and when the influence of dark energy was still negligible. Complementary information from later cosmic times are therefore essential. This information can come from type Ia supernovae, galaxy clusters, gravitational lensing or cosmic shear, and baryon acoustic oscillations (BAO), and the imprint of the CMB power spectrum, which is still discernible at moderate redshifts (e.g. Cardone et al. (2002); Treu & Koopmans (2002); Bonamente et al. (2006); Suyu et al. (2012)).

All of these data provide distances and linear scales at significant redshifts. However, it is the local universe where dark energy is dominant. Thus the local Hubble constant, H_0 , provides the largest “lever arm” with respect to the CMB for determining the equation of state of dark energy. The use of Cepheids (e.g. Freedman et al. (2001); Sandage et al. (2006)) as well as the combined use of Cepheids and Type Ia supernovae (e.g. Riess et al. (2011)) has traditionally dominated determinations of H_0 . What is missing, however, are direct geometric distance estimates that do not require a complex and uncertain ladder of calibration of “standard candles.”

Direct geometric distance measurements to water masers in nuclear regions of galaxies that are well into the Hubble flow (roughly > 30 Mpc distant) provide a promising new and independent method for refining the value of H_0 . Observations of water masers in accretion disks within ~ 0.1 pc of a galaxy’s central supermassive black hole have been used to measure angular-diameter distances to galaxies, independently of other techniques that often rely on standard candles. Very Long Baseline Array (VLBA) observations of the H_2O masers in the nearby Seyfert 2 galaxy NGC 4258 established the technique and provided an accurate, angular-diameter distance of 7.2 ± 0.5 Mpc to the galaxy (Herrnstein et al. 1999). This galaxy is too close to permit a direct measurement of H_0 (i.e. by dividing its recessional speed by its distance), since its (uncertain) peculiar velocity could be a large fraction of its recessional speed. However, NGC 4258 has proven extremely valuable as a solid anchor for the extragalactic distance scale (Freedman et al. 2001; Riess et al. 2011).

Recently, the Megamaser Cosmology Project (MCP) reported a distance to UGC 3789, another galaxy with water masers in a nuclear accretion disk, of 49.9 ± 7.0 Mpc (Reid et al. 2009; Braatz et al. 2010) (hereafter Papers I and II). This galaxy has a recessional velocity of 3481 km s^{-1} (relativistically corrected and with respect to the cosmic microwave background), which includes its peculiar velocity of $-151 \pm 163 \text{ km s}^{-1}$ based on galaxy flow models of Masters et al. (2006) and Springob et al. (2007)). Combining the recessional

velocity and distance yielded $H_0 = 69 \pm 11 \text{ km s}^{-1} \text{ Mpc}^{-1}$.

Since UGC 3789 is well into the Hubble flow it can provide a direct estimate of H_0 with a potential uncertainty as small as $\pm 5\%$, limited by the uncertainty in its peculiar motion. Therefore, since reporting our initial results, we have conducted additional observations of UGC 3789, in order to reduce the uncertainty of the H_0 estimate. In total, we have now analyzed nine VLBI observations, using the NRAO ¹ 10-antenna VLBA, the 100-m Green Bank Telescope (GBT) and the 100-m Effelsberg ² telescope. The VLBI observations are reported in §2. We have also extended our monitoring of changes in the water maser spectrum with monthly (except during the humid summer) observations with the GBT for a period spanning 5.5 years. These spectra are documented in §3 and used to determine the accelerations of individual maser features. In §4, we describe a Bayesian approach for fitting a model of the accretion disk to these data. The model allows for a warped disk with eccentric gas orbits and includes parameters for the central (black hole) mass and position, as well as for H_0 .

2. VLBI Imaging

VLBI observations were conducted on nine epochs (NRAO program codes BB227A, BB227B, BB242A, BB242I, BB242K, BB242L, BB242Q, BB261G, and BB261S) between December 2007 and April 2010. Six of the nine observations yielded maps with signal-to-noise ratios degraded by factors of two or greater owing to the loss of one of the 100-m telescopes (usually to poor weather) or the weakening of the peak maser emission to levels where self-calibration using the maser emission (phase-referencing) was poor. The three epochs with excellent weather, antenna performance, and strong maser emission included BB227A (2007 December 7; reported in Paper I), BB242L (2008 December 12), and BB261G (2009 April 11). Only results from these epochs are reported here.

We observed with 16-MHz bands covering five frequencies, three in dual polarization and two in single polarization. In our early observations, these bands were centered at (optical definition) local standard of rest (LSR) velocities (and polarizations) of 3880.0 (LCP & RCP), 3710.0 (LCP), 3265.0 (LCP & RCP), 2670.0 (LCP & RCP), and 2500.0 (LCP) km s^{-1} for BB227A; for the BB242L and BB261G, we shifted the center velocities of the fourth and fifth bands to 2717.6 and 2513.6 km s^{-1} , in order to map new maser features not covered

¹The National Radio Astronomy Observatory is operated by Associated Universities, Inc., under a cooperative agreement with the National Science Foundation.

²The Effelsberg 100-m telescope is a facility of the Max-Planck-Institut für Radioastronomie

in the original setup. The data for each polarization of each band were cross-correlated with 128 spectral channels, yielding channels separated by 1.7 km s^{-1} .

Generally, the data were analyzed as described in Reid et al. (2009). The final calibration step involved selecting a maser feature as the interferometer phase-reference, and details of this procedure varied among epochs depending on maser strength and interferometer coherence times. The strongest maser feature in the spectrum usually peaked at $\approx 0.07 \text{ Jy}$ and was fairly broad. For BB227A, we averaged five spectral channels spanning an LSR velocity range of 2685 to 2692 km s^{-1} (i.e. channels 52 to 56 from the blue-shifted high-velocity band centered at $V_{\text{LSR}} = 2670 \text{ km s}^{-1}$), adding together the data from both polarizations, and fitting fringes over a 1 min period. For BB242L, we averaged 13 spectral channels spanning an LSR velocity range of 2682 to 2702 km s^{-1} (i.e. channels 74 to 86 from the blue-shifted high velocity band centered at $V_{\text{LSR}} = 2717.6 \text{ km s}^{-1}$) and fitted fringes over a 2 min period. For BB261G, we averaged 7 spectral channels spanning an LSR velocity range of 2685 to 2696 km s^{-1} (i.e. channels 78 to 84 from the blue-shifted high velocity band centered at $V_{\text{LSR}} = 2717.6 \text{ km s}^{-1}$), again with 2 min averaging.

After calibration, we Fourier transformed the gridded (u,v) -data to make images of the maser emission in all spectral channels for each of the five IF bands. The images were deconvolved with the point-source response using the CLEAN algorithm and restored with a circular Gaussian beam with a 0.30 mas full-width at half-maximum (approximately matching the geometric mean of the dirty beam). The rms noise levels in channel maps were $\approx 1 \text{ mJy}$. All images appeared to contain single, point-like maser spots. We then fitted each spectral-channel image with an elliptical Gaussian brightness distribution in order to obtain positions and flux densities.

Spectral images for the three epochs are shown in Fig. 1. These images show nearly the identical spatial-velocity pattern of maser emission. This is expected as material in near-circular orbit in the accretion disk at the average masing radius has an orbital period of $\sim 1000 \text{ yr}$ and thus rotates by only about 0.5 degrees of disk azimuth between the first and last observation. Most of the spatial scatter in the images is from measurement uncertainty, primarily from signal-to-noise limitations, of $\approx 25 \mu\text{as}$ for weaker features of $\approx 10 \text{ mJy}$.

3. GBT Spectral Monitoring and Acceleration Fitting

Paper II describes the procedures used to monitor the H_2O maser spectrum of UGC 3789 from January 2006 to March 2009 with the GBT. We continued these observations through June 2011. Typically, observations were conducted at monthly intervals for nine months per

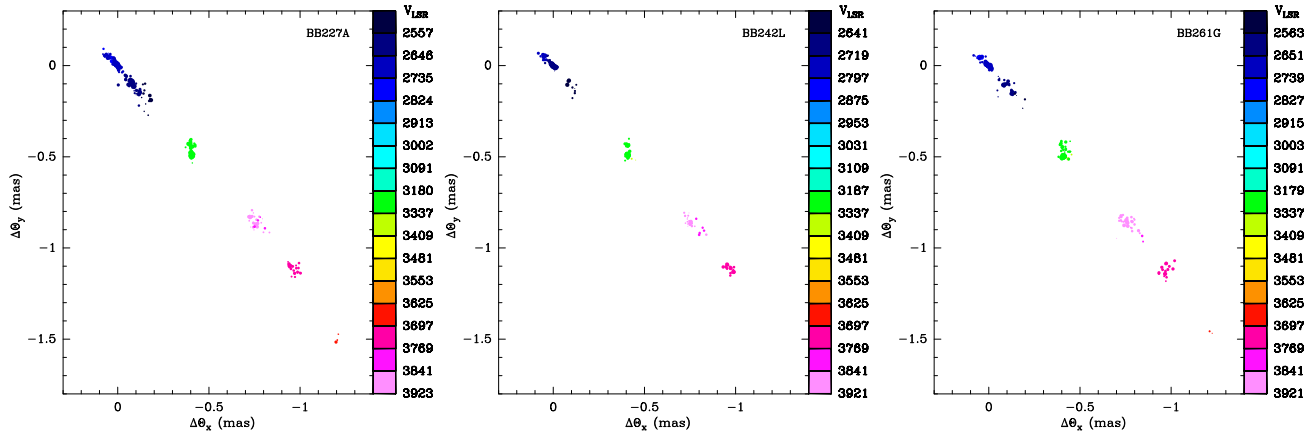


Fig. 1.— Maps of the 22 GHz H_2O masers toward UGC 3789 constructed from VLBI data using the VLBA, the GBT and the Effelsberg antennas for programs BB227A (2007 December 7), BB242L (2008 December 12) and BB261G (2009 April 11). The LSR velocity of each maser spot is indicated by the color bar on the right side of each panel.

year, avoiding the summer when atmospheric water vapor precluded sensitive observations. These spectra were divided into 6 yearly blocks and analyzed to determine velocity drifts (accelerations) of individual maser features.

Measurement of the acceleration of systemic-velocity masers is key to determining the angular-diameter distance of the galaxy. In principle, accelerations are straight-forwardly obtained from the linear drift in peak velocity with time. In practice, however, blending of adjacent spectral features, coupled with modest signal-to-noise ratio observations, makes this difficult. We applied two methods to measure accelerations.

3.1. Method–1

In Paper II we measured accelerations in two steps. First, we identified spectral peaks in individual spectra “by eye” and tracked these peak velocities over time to obtain preliminary accelerations. Then, we modeled the spectral flux density as a function of velocity and time as the sum of a number of Gaussian spectral lines, whose center velocity changes linearly with time. We repeated this approach with the extended spectral monitoring data.

Parameters for individual Gaussian components included the amplitudes (one per observational epoch), the line width, and the center velocity (at a reference epoch) and its (linear) change in velocity over time. Initial values for maser component velocities and accelerations were set based on the “by eye” values; line widths were initially set at 2.0 km s^{-1} and

assumed not to vary over the ≈ 9 months of observations being analyzed. Initial values for maser component amplitudes for each observation were set automatically at the flux density of each spectrum at the velocity determined by the initial central velocity and acceleration parameters.

The parameters were adjusted by a sequence of least-square fitting (to minimize the sum of the squares of the weighted post-fit residuals or χ^2). In the first fitting step, only the amplitudes were adjusted. Next, the amplitudes, central velocities and line widths were adjusted, using parameter values derived from the first fits. Finally, all parameters (including accelerations) were allowed to vary. While this least-squares approach works well and gives accelerations that largely agree with those visually evident in the spectra, it is time-consuming process and dependent on somewhat subjectively determined initial parameters.

3.2. Method–2

In order to avoid setting the initial velocities and acceleration parameters by eye, we developed an alternative analysis method. This method involved randomly choosing initial values followed by least-squares fitting and evaluation of the quality of each fit. We repeated this process, with independently chosen initial parameter values, about 100 times and recorded the four fits with the lowest values of χ^2 per degree of freedom. In detail, for each trial solution, we assigned the center velocity, V_n , of the n^{th} spectral component by selecting a velocity offset randomly from a Gaussian distribution with a mean of 2.0 km s^{-1} and a standard deviation of 0.7 km s^{-1} and adding this offset to the central velocity of the $(n-1)^{\text{th}}$ component. We started at the low end of the velocity “window” being fitted and continued until we reached the high end; this allowed different trial fits to have different numbers of velocity components.

Since the change in component acceleration with velocity is generally small, rather than set accelerations independently for each component as in method–1, we set a single acceleration and its velocity derivative (2 parameters) for the entire velocity window under consideration. This minimizes the number of free parameters, but requires setting small velocity windows over which component accelerations are nearly constant. Specifically, we assigned an initial acceleration, A_n , to the n^{th} velocity component given by $A_n = A_c + (dA/dV)(V_n - V_c)$, where V_c is the center of the velocity window, A_c is the average acceleration over the fitting window and dA/dV allows for a linear change in acceleration with velocity. Values of A_c were chosen randomly from a Gaussian distribution, whose mean was estimated from the fits described in method–1 and whose standard deviation, σ_A , was one-third of that

mean. Values of dA/dV were chosen in a similar random manner from a distribution with zero mean and standard deviation of σ_A . The combined effect of the large standard deviation for accelerations and allowance for a linear change in acceleration with velocity resulted in broad sampling of initial acceleration parameter space.

3.3. Acceleration Fitting Results

For systemic velocity features, we used three velocity windows for acceleration fitting: 3230–3280, 3286–3316, and 3350–3370 km s^{-1} , since emission outside of these windows was generally absent or very weak (< 5 mJy). Maser features in UGC 3789 typically have lifetimes (with flux densities > 5 mJy) of ~ 6 to 12 months. Therefore, we fitted accelerations separately to groups of ≈ 9 consecutive monthly spectra (from fall through spring) covering 5.5 years and centered at ≈ 2008.8 . These observations well-covered the VLBI imaging observations, whose mean epoch was ≈ 2008.7 .

Yearly acceleration measurements generally were consistent with a single value, although for some velocity ranges there was considerable scatter (up to about $\pm 30\%$ for maser near 3290 km s^{-1}). Because of this, and the expectation of small changes in acceleration over our observing period (as masing clouds move by less than 0.5 degrees of disk azimuth), we velocity binned and averaged the fitted accelerations from the 6 “yearly” groups of spectra. Variance weighted averages of acceleration as a function of velocity for the systemic features are plotted Fig. 2 for both fitting methods outlined above.

The results for method–1 are plotted with filled (red) circles in Fig. 2. There is moderate scatter among the accelerations within each velocity window, and this scatter greatly exceeds that expected from the formal acceleration uncertainties. This reflects the complexity caused by the velocity-blending and moderate signal-to-noise ratio of individual spectra. However, the average values in each window are well determined and, especially, in the 3230–3280 window, there is a smooth change in acceleration with velocity.

In order to provide an independent check on the results from method–1, we re-fitted the spectra using method–2. For this method we randomly chose initial values for the maser feature parameters and conducted ≈ 100 independent trial fits. For each velocity window and each “yearly” time group, we selected the four trial fits with the lowest χ^2 values. We then binned all results in 2 km s^{-1} bins and calculated a weighted average acceleration for each velocity bin. These results are plotted in Fig. 2 with open (blue) squares. There is very good agreement between the two methods; the average accelerations in each velocity window are nearly identical. The small difference between the slopes of A vs. V_{LSR} is within

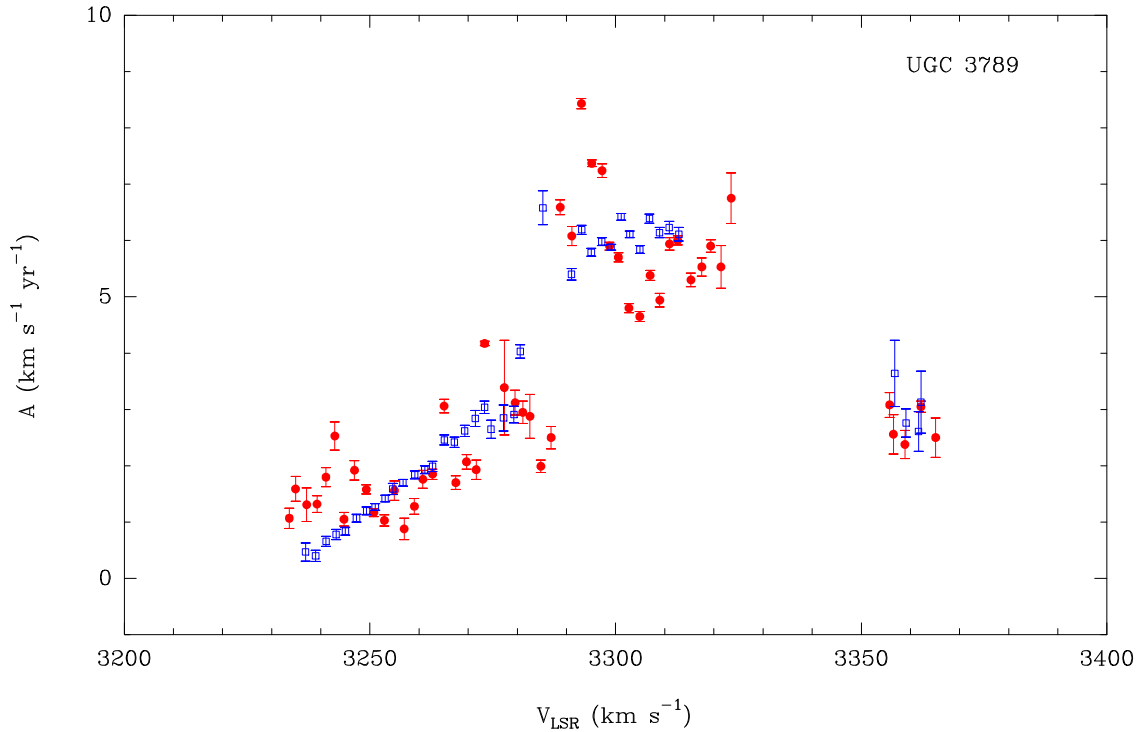


Fig. 2.— Acceleration measurements as a function of LSR velocity for systemic velocity maser features. *Filled red circles* are results from method-1 (see §3.1) and *open blue squares* are from method-2 (see §3.2).

statistical uncertainty. We conclude that the accelerations given by the solid (red) points in Fig. 2 are near optimum values and are not biased by the choice of initial parameter values in the first step of method-1.

Acceleration measurements for high velocity features are considerably less complicated as these features are not highly blended and have small changes in velocity over time. Therefore, we only used method-1 (described in §3.1) for these features, and fitted accelerations are given in Table 1. The precise values of these accelerations have almost no effect on distance (H_0) estimation; indeed one could replace them with zero with little effect on H_0 .

4. Modeling the Accretion Disk & Estimating H_0

The position/velocity measurements from the three VLBI maps were combined by binning the velocities in 2.0 km s^{-1} wide bins (comparable to maser linewidths) and calculating a variance weighted position and velocity. We associated these positions and velocities with maser feature accelerations, from the GBT time monitoring of spectra, by choosing the VLBI velocity closest to that of an acceleration fit. As there are fewer acceleration fits than

VLBI position/velocity measurements, not all VLBI measurements have corresponding accelerations. This procedure yielded a data set that can be modeled and H_0 estimated. The velocity, position and acceleration values are given in Table 1.

Rather than use formal fitting uncertainties, which tend to be optimistic, we adopted more realistic “error floors” for the data uncertainties of ± 0.01 mas for positions, ± 1.0 and ± 0.3 km s⁻¹ for the velocities of systemic and high-velocity maser features, respectively, and ± 0.57 km s⁻¹ yr⁻¹ for accelerations. Error floors were added in quadrature to formal fitting uncertainties. For example, systematic errors of ≈ 0.01 mas between systemic and high velocity features can be caused by an error in the absolute position of the reference maser spot of a few mas (Argon et al. 2007). Using error floors allows not only for systematic uncertainty not captured by formal estimates, but also for “astrophysical noise” in the accretion disk, such as could come from spiral structure. Such astrophysical noise is seen in the nearby, well-studied, disk of NGC 4258 at levels of ≈ 0.5 km s⁻¹ yr⁻¹ for systemic features accelerations (Humphreys et al. 2008). In §4.1, we explore the sensitivity of the fitted parameters to changes in the magnitudes of these error floors.

Conceptually, were the masers in a perfectly thin and flat accretion disk orbiting circularly about a point mass and viewed edge-on, the position-velocity data for the high velocity features would trace a Keplerian profile (i.e. $V = \sqrt{GM/r}$), where G is the gravitation constant, M is the mass of the central black hole, and r is the distance of a masing cloud from the the black hole. The symmetry of the approaching and receding features can be used precisely locate the central black hole both in position (x_0, y_0) and velocity (V_0) . Thus, for high velocity features that are in the plane of the sky, the VLBI image directly gives a feature’s angular radius, $\theta = r/D$, where D is the distance to the galaxy. Systemic velocity masers in front of the black hole, moving transversely on the sky, display a change in velocity over time (A) as they orbit the central mass. Features in a thin annulus at radius, r , will be observed to accelerate at $A = V^2/r$. Thus, from position-velocity and acceleration measurements, one can estimate $D = V^2/A\theta$ and then $H_0 = V_0/D$. Note that proper motions of systemic-velocity masers can also be used to estimate distance. However, proper motions decreases in magnitude with source distance and are generally far less accurate than radial acceleration measurements based on changing Doppler shifts (which are distance independent).

In practice, accretion disks are somewhat more complicated than the idealized case just described. The disks are not precisely edge-on (although strong maser amplification prefers disk spin axes to be within about 5° of the plane of the sky), disks are often somewhat warped, and gas may be on somewhat eccentric orbits. Also, galaxies typically have peculiar motions of ~ 100 km s⁻¹ with respect to a pure Hubble flow. These complications are best addressed by constructing a model for maser orbits in the disk and adjusting the model

parameters to best match the observations. We modeled the system with up to 15 global parameters. The central black hole has a mass, M , is located at (x_0, y_0) on the sky (relative to the reference maser feature) and has a line-of-sight velocity, V_0 . Following Herrnstein et al. (1999), we model the disk warp by a change in inclination with radius, $i(r) = i_0 + (\partial i/\partial r)\delta r + (\partial^2 i/\partial r^2)\delta r^2$, and position angle (defined east of north) with radius, $p(r) = p_0 + (\partial p/\partial r)\delta r + (\partial^2 p/\partial r^2)\delta r^2$, where $\delta r = r - r_{ref}$ and r_{ref} is a reference radius assigned to the middle of the maser distribution. Our model can allow the masers to have eccentric orbits, with eccentricity e and pericenter rotated in angle $\omega = \omega_0 + (\partial\omega/\partial r)r$ with respect to our line of sight. Finally, the galaxy distance is derived by assuming its radial motion deviates from a pure Hubble flow, given by H_0 , with a peculiar velocity V_p relative to the cosmic microwave background reference frame.

We chose to estimate H_0 directly, rather than fit first for D , followed by a second step to estimate H_0 . There are two advantages in our approach. Firstly, unlike for NGC 4258 which is not sufficiently distant to be in the Hubble flow and hence cannot be used to accurately estimate H_0 , for UGC 3789 our primary interest is H_0 and not D . Secondly, when solving for D , systemic feature accelerations, which are the least accurately measured type of data, appear in the denominator ($D = V^2/A\theta$) and lead to asymmetric posteriori probability distributions and complicate error estimation for H_0 .

In addition to the global parameters, each maser feature requires two parameters, its radius, r , and azimuth, ϕ , to specify its location in the disk. Initial values for r and ϕ for high-velocity features were estimated from the position data, assuming $\phi = 90^\circ$ for red-shifted features and $\phi = -90^\circ$ for blue-shifted features. Systemic velocity features were assigned initial r values based on the acceleration data and ϕ values based on velocity data. All (r, ϕ) parameters were assigned flat priors and were adjusted in the fitting process.

We evaluated parameter *posteriori* probability distributions with Markov chain Monte Carlo (MCMC) trials that were accepted or rejected according to the Metropolis-Hastings algorithm. Parameters were assigned prior values and uncertainties. All parameters except for one were given flat priors and hence could vary freely, constrained only by the difference between data and model. The only parameter with a constraining prior was the galaxy’s peculiar velocity, $V_p = 211 \pm 163 \text{ km s}^{-1}$; this comes from the sum of two values: one value is expected from large scale gravitational perturbations (Masters et al. 2006; Springob et al. 2007) which are expected to cause observed velocities for UGC 3789 to be lower by $151 \pm 163 \text{ km s}^{-1}$ with respect to the Hubble flow; the second value is from a (known) correction of 60 km s^{-1} to transform from the LSR to the cosmic microwave background reference frame. All velocities quote here are non-relativistic, optical definition, LSR velocities; these parameters and the data were converted internally in the fitting program to relativistically

correct values.

Initial runs indicated very little warping (as is evident in the VLBI images) and maser orbital eccentricities near zero. Hence, for our “basic model,” we used only the first order warping parameters and assumed circular gas orbits. We ran 20 “burn-in” stages, each with 10^5 trials, in order to arrive at near optimum parameter values. After each stage we adjusted individual parameter step sizes to come from Gaussian distributions with a similar widths as the anticipated *posteriori* probability distributions, multiplies by a global step-size factor. This factor was also adjusted in the burn-in stages to scale parameter steps so that an optimal Metropolis-Hastings acceptance rate of $\approx 23\%$ was achieved; this factor was found to be ≈ 0.01 .

After discarding the burn-in stage trials, we evaluated 10^7 McMC trials to obtain final *posteriori* probability distributions. We found a significant correlation coefficient of ≈ 0.87 between the Hubble constant (H_0) and central black hole mass (M) parameters. In order to more optimally sample the probability distributions for these parameters, we modified the McMC values for these two parameters to be totally correlated for 50% of the trials and uncorrelated 50% for the remainder (Gregory 2011).

From Bayes’ theorem the probability of the data (d) given a model (m) and priors (I), is given by

$$P(d|m, I) \propto P(m|d, I) \times P(m|I) .$$

Since we assume Gaussianly distributed uncertainties for the data and priors, maximizing $P(m|d, I) \times P(m|I)$ is equivalent to minimizing $\chi_d^2 + \chi_m^2$, where the subscripts d and m refer to the data and model (given the priors), respectively. The best-fitting trial gave $\chi_d^2 = 1.473$ for 227 degrees of freedom. In Fig. 3, we show projections of the data with the best-fitting model superposed. The modeling also yields the (r, ϕ) coordinates of each maser feature in the disk plane, which are displayed in Fig. 4 (neglecting the slight warping of the disk).

Optimum values of the model parameters are given in Table 2. These were estimated from the *posteriori* probability distributions marginalized over all the other parameters. They were generated from the 10^7 McMC trials by producing binned histograms and finding the mode and $\pm 34\%$ ($\approx \pm 1\sigma$) ranges. Of some interest is the very accurate estimate of the mass of the central black hole of $(1.11 \pm 0.08) \times 10^7 M_\odot$.

The binned *posteriori* probability distribution for the Hubble constant, marginalized over all other parameters, is displayed in Fig. 5. This distribution can be well approximated by a Gaussian with a mean of $71.6 \text{ km s}^{-1} \text{ Mpc}^{-1}$ and a 68% confidence range of $\pm 5.0 \text{ km s}^{-1} \text{ Mpc}^{-1}$. Allowing for a 163 km s^{-1} uncertainty in the peculiar velocity of UGC 3789 slightly increases the total uncertainty of H_0 to $\pm 5.7 \text{ km s}^{-1} \text{ Mpc}^{-1}$. This Hubble constant,

coupled with the recessional velocity of 3455 km s^{-1} (relativistic, relative to the CMB, and corrected for a peculiar velocity of -151 km s^{-1}) and assuming a cosmological matter density parameter $\Omega_m = 0.27$, places UGC 3789 at a distance of $47.6 \pm 4.0 \text{ Mpc}$.

4.1. Sensitivity of H_0 to Data Weighting

We tested the sensitivity of our estimate of H_0 to significant ($> 30\%$) changes in the error floors applied to the data set of Table 1. Changing the positional error floors from 0.010 to 0.005 or 0.015 mas changed estimates of H_0 by less than $1 \text{ km s}^{-1} \text{ Mpc}^{-1}$. Varying the acceleration error floor from 0.57 to 0.27 or 0.87 $\text{km s}^{-1} \text{ yr}^{-1}$ produced similarly small changes in H_0 . Decreasing the velocity error floors for the systemic and high-velocity maser features from 1.0 and 0.3 km s^{-1} , respectively, to 0.7 and 0.2 km s^{-1} also yielded insignificant changes in H_0 .

In our tests, the only sensitivity of H_0 to changes in error floors occurred when increasing the velocity error floors for systemic and high-velocity maser features from 1.0 and 0.3 km s^{-1} , respectively, to 1.3 and 0.4 km s^{-1} . This resulted in estimates of H_0 reduced by 4 $\text{km s}^{-1} \text{ Mpc}^{-1}$. This small sensitivity likely comes from down-weighting the velocity information in the high-velocity masers. This information is critical to the method as it provides direct and strong constraints for the location (x_0, y_0) and velocity (V_0) of the central black hole. Down-weighting this data, by increasing its uncertainty, requires the program to use weaker, indirect information in the position/acceleration data to determine these parameters.

4.2. Secondary χ^2 Minima

In preliminary attempts to fit the data, we used a “loose” prior for H_0 of $72 \pm 12 \text{ km s}^{-1} \text{ Mpc}^{-1}$, probably at least double the current uncertainty in the Hubble Constant. However, we ultimately dropped this constraint in favor of a flat prior on H_0 , allowing us to arrive at an estimate of H_0 from UGC 3789 data alone that is independent of prior knowledge. We then tested the sensitivity of the estimates of H_0 to the initial values. Starting with H_0 values as high as $80 \text{ km s}^{-1} \text{ Mpc}^{-1}$, we found fitted values returning close to our base result of $71.6 \text{ km s}^{-1} \text{ Mpc}^{-1}$. However, starting H_0 below $60 \text{ km s}^{-1} \text{ Mpc}^{-1}$, we found a stable fit with $H_0 = 59 \text{ km s}^{-1} \text{ Mpc}^{-1}$.

The $H_0 = 59 \text{ km s}^{-1} \text{ Mpc}^{-1}$ result likely comes from a secondary minimum in χ^2 space. In order to compare χ^2 values, we held the global parameters constant and re-fit only for the (r, ϕ) values for each maser feature. These fits returned $\chi^2 = 352.1$ (for 227 degrees of

freedom) for $H_0 = 59$, compared with the better $\chi^2 = 340.5$ (for the same 227 degrees of freedom) for our basic fit with $H_0 = 71.6 \text{ km s}^{-1} \text{ Mpc}^{-1}$. We rule out the $H_0 = 59 \text{ km s}^{-1} \text{ Mpc}^{-1}$ fit because it produces a worse χ^2 and is outside realistic bounds for the Hubble Constant.

4.3. Eccentric Gas Orbits

In order to assess the sensitivity of H_0 estimates to the assumption of circular gas orbits used in our basic model, we re-fit the data with a more general model with 3 additional parameters (e, ω and $\partial\omega/\partial r$) that allow eccentric gas orbits with pericentric angle changing linearly with radius in the accretion disk. Best-fit values for eccentricity were very small, 0.025 ± 0.008 , with pericenter at $-60^\circ \pm 20^\circ$ disk azimuth. Such a small eccentricity has a negligible effect on the other parameters estimates.

5. Conclusions

The H_2O masers in an accretion disk orbiting the supermassive black hole at the center of the UGC 3789 provide an excellent opportunity to measure the angular-diameter distance of the galaxy directly and with high accuracy. Since UGC 3789 is expected to have a low peculiar velocity with respect to the Hubble flow of $< 200 \text{ km s}^{-1}$, one can obtain a direct measurement of H_0 with high accuracy. Such measurements are the central goal of the Megamaser Cosmology Project, which aims to determine H_0 with $\pm 3\%$ accuracy.

We have presented the results of multi-epoch VLBI imaging and over 5 years of spectral monitoring with the GBT. We determine H_0 to be $71.6 \pm 5.7 \text{ km s}^{-1} \text{ Mpc}^{-1}$, which includes sources of systematic error. Direct measurements of H_0 , such as from UGC 3789, are especially important for constraining the equation of state of dark energy, w , since the effects of dark energy are greatest at the present epoch. Thus, for example, our measurement of H_0 with 8% accuracy provides a comparable constraint on w as a 5% accurate measurement at $z \approx 0.35$ (e.g. from baryon acoustic oscillations (Eisenstein et al. 2005)).

Facilities: VLBA, GBT, Effelsberg

REFERENCES

- Argon, A. L., Greenhill, L. J., Reid, M. J., Moran, J. M. & Humphreys, E. M. L. 2007, *ApJ*, 659, 1040
- Braatz, J. A., Reid, M. J., Humphreys, E. M. L., et al. 2010, *ApJ*, 718, 657
- Bonamente, M., Joy, M. K., LaRoque, S. J., Carlstrom, J. E., Reese, E. D. & Dawson, K. S. 2006, *ApJ*, 647, 25
- Cardone, V. F., Capozziello, S., Re, V. & Piedipalumbo, E. 2002, *A&A*, 382, 792
- Eisenstein, D. J., Zehavi, I., Hogg, D. W. et al. 2005, *ApJ*, 633, 560
- Freedman, W. et al. 2001, *ApJ*, 553, 47
- Gregory, P. C. 2011, *MNRAS*, 410, 94
- Herrnstein et al. 1999, *Nature*, 400, 539
- Humphreys, E. M. L., Reid, M. J., Greenhill, L. J., Moran, J. M. & Argon, A. L. 2008, *ApJ*, 672, 800
- Komatsu, E. Smith, K. M., Dunkley, J., et al. 2011, *ApJS*, 192, 18
- Masters, K. L., Springob, C. M., Haynes, M. P., et al. 2006, *ApJ*, 653, 861
- Reid, M. J., Braatz, J. A., Condon, J. J., et al. 2009, *ApJ*, 695, 287
- Riess, A. G., Macri, L., Casertano, S., et al. 2011, *ApJ*, 730, 119
- Sandage, A., Tammann, G. A., Saha, A., Reindl, B., Macchetto, F. D. & Panagia, N. 2006, *ApJ*, 653, 843
- Sivia, D. & Skilling, J. 2006, “Data Analysis: A Bayesian Tutorial, 2nd Edition, (New York, Oxford Univ. Press Inc.), 168.
- Springob, C. M., Masters, K. L., Haynes, M. P. et al. 2007, *ApJS*, 172, 599
- Suyu, S. H., Hensel, S. W., McKean, J. P. et al. 2012, *ApJ*, 750, 10
- Treu, T. & Koopmans, L. V. E. 2002, *MNRAS*, 337, 6

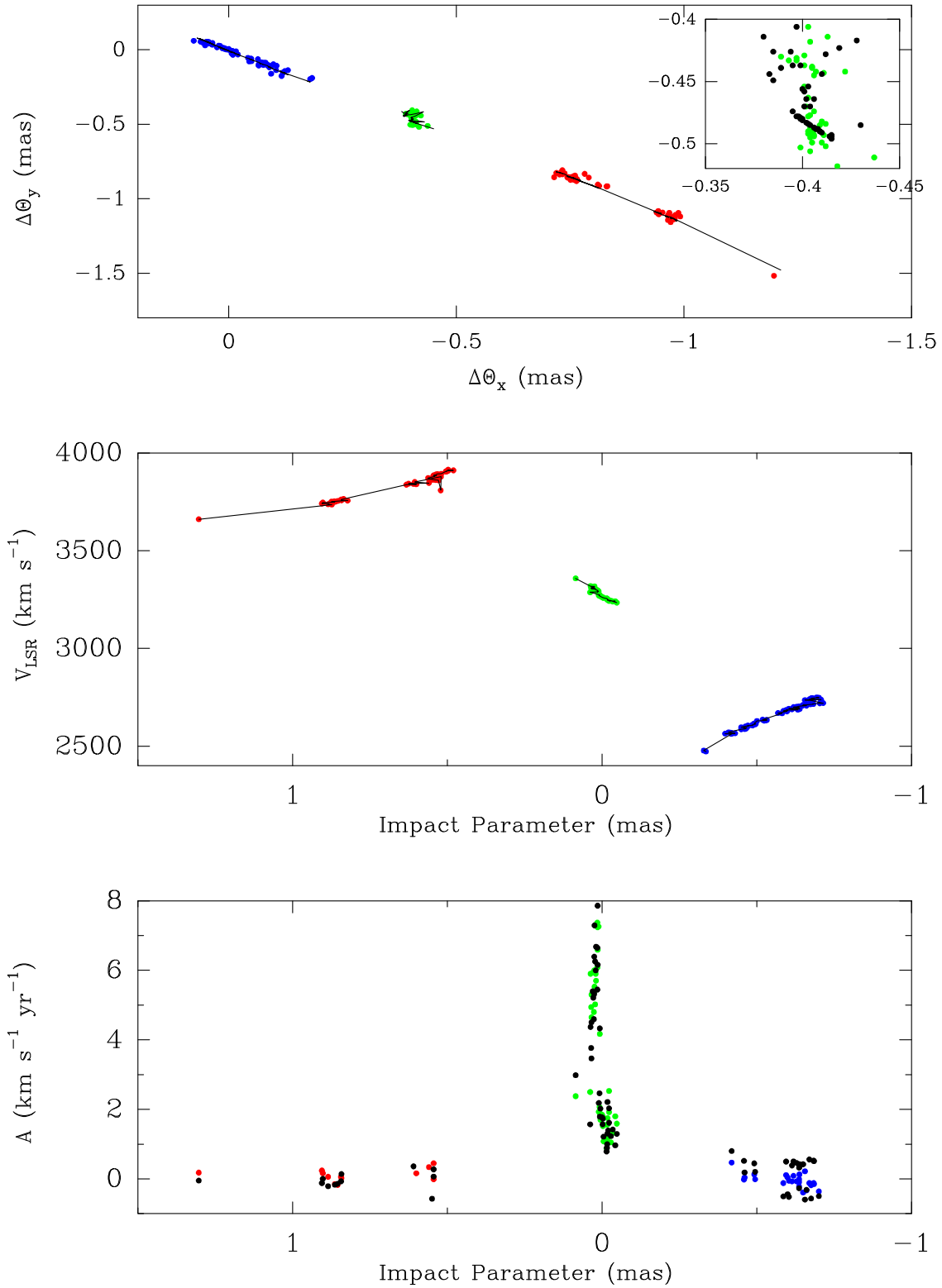


Fig. 3.— Data (colored dots) and best-fit model (lines and black dots). *Top panel:* Positions on the sky. Inset shows a blow-up of the systemic-velocity masers. *Middle panel:* LSR velocity versus position along the disk. *Bottom panel:* Accelerations versus impact parameter.

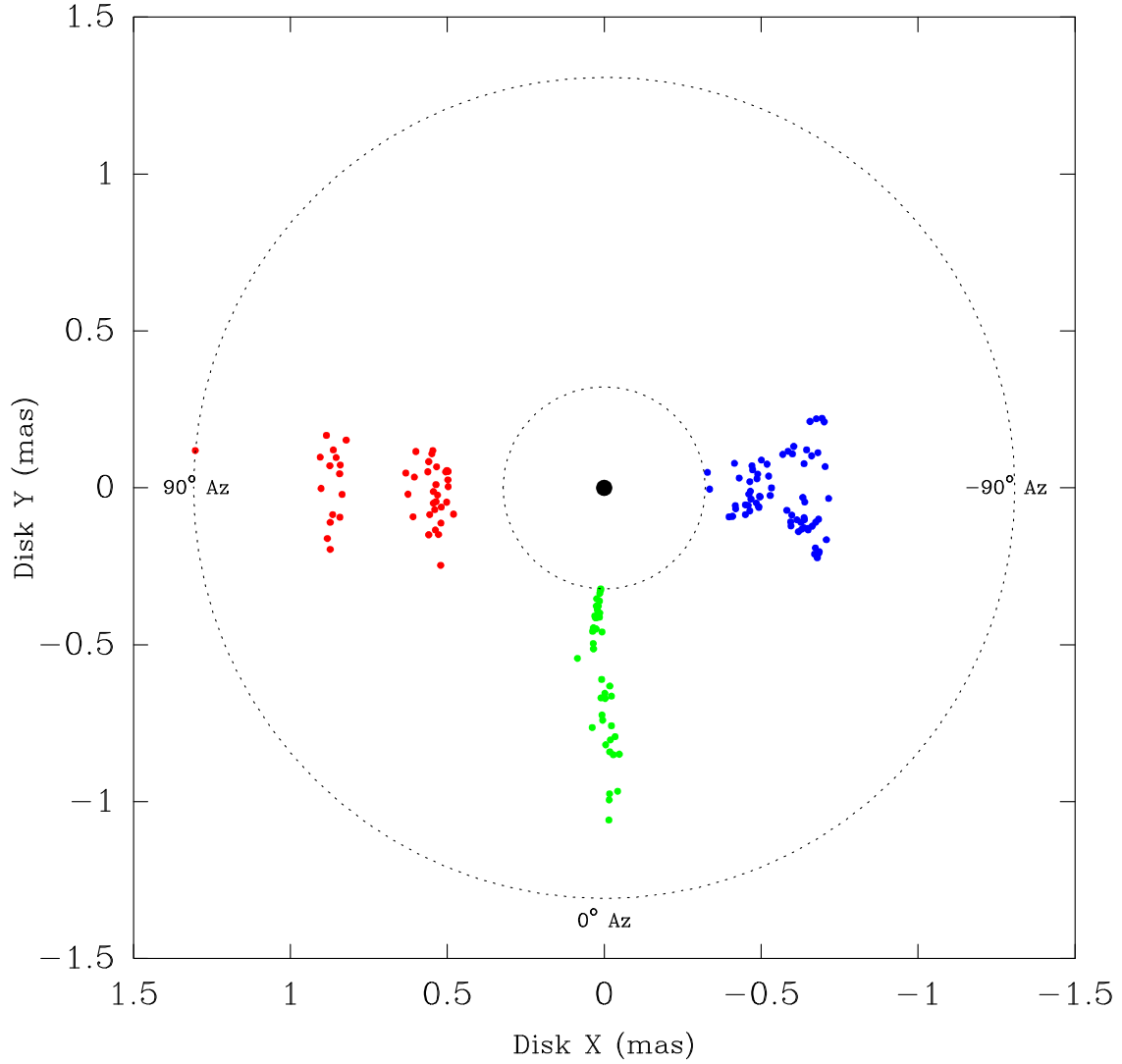


Fig. 4.— Location of maser features projected in the plane of the accretion disk based on the best-fit model. The location of the central black hole is shown with a *black filled circle* at the origin. The observer is at a large negative Y location. Disk azimuth defined is as 0° toward the observer. *Red and Blue* dots indicate the red-shifted (toward disk azimuth $\approx 90^\circ$) and blue-shifted (toward disk azimuth $\approx -90^\circ$) high-velocity masers, respectively. *Green* dots indicate the systemic velocity masers (toward disk azimuth $\approx 0^\circ$).

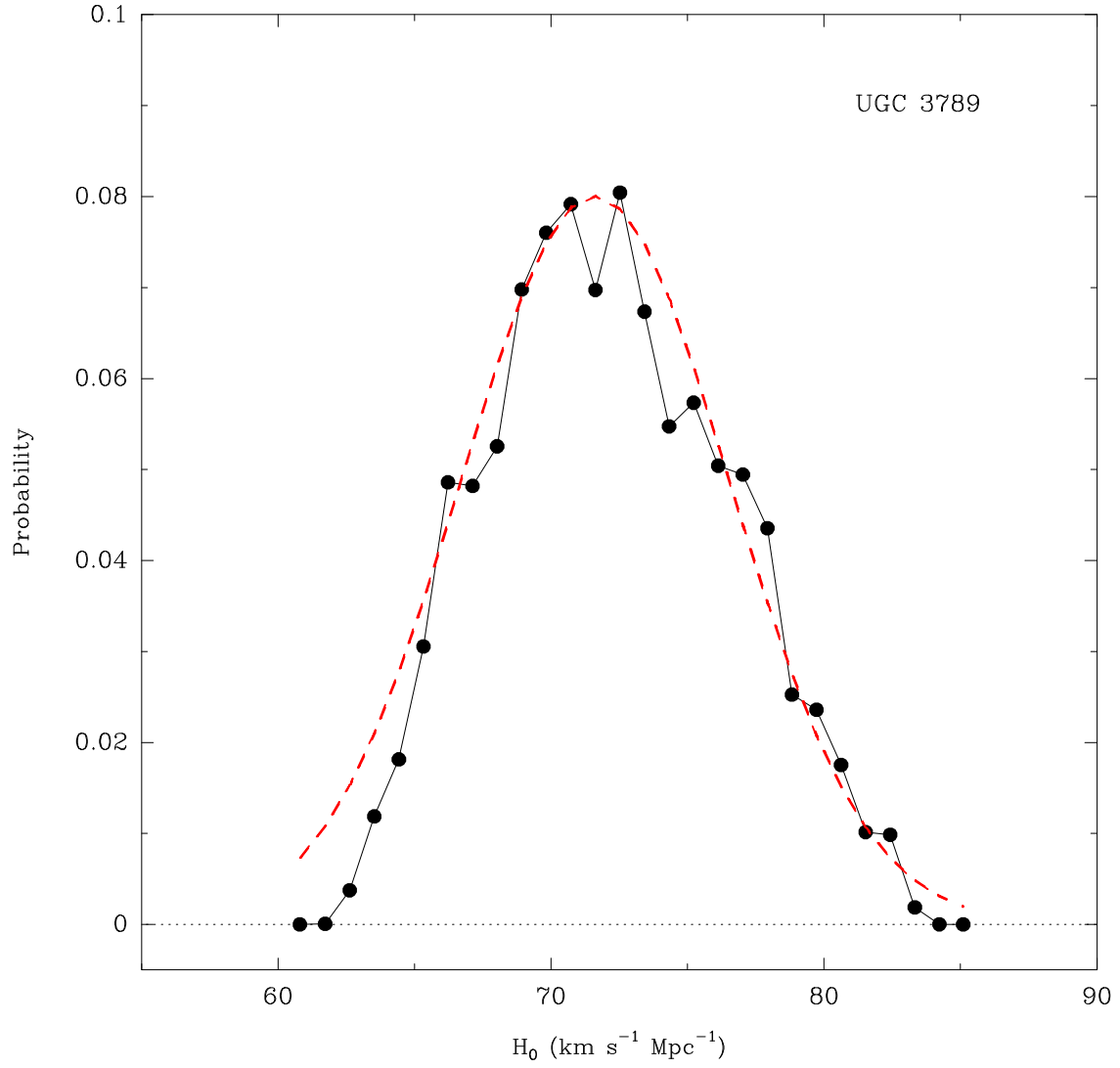


Fig. 5.— Posterior probability distribution for the Hubble constant parameter (H_0), marginalized over all other parameters. Superposed (*dashed red line*) is a Gaussian with $\sigma = 5 \text{ km s}^{-1} \text{Mpc}^{-1}$.

Table 1. UGC 3789 H₂O Maser Data

V_{LSR} (km s ⁻¹)	Θ_x (mas)	σ_{Θ_x} (mas)	Θ_y (mas)	σ_{Θ_y} (mas)	A (km s ⁻¹ yr ⁻¹)	σ_A (km s ⁻¹ yr ⁻¹)
2472.8	-0.183	0.009	-0.190	0.009
2477.9	-0.179	0.008	-0.197	0.021
2562.9	-0.116	0.005	-0.176	0.028
2564.6	-0.119	0.004	-0.153	0.005
2566.3	-0.122	0.003	-0.149	0.003
2568.0	-0.123	0.003	-0.143	0.009	0.5	0.2
2569.7	-0.130	0.009	-0.137	0.007
2571.4	-0.093	0.020	-0.161	0.008
2586.7	-0.104	0.012	-0.137	0.012
2588.4	-0.089	0.004	-0.118	0.003	0.0	0.2
2590.1	-0.084	0.009	-0.102	0.005
2591.8	-0.087	0.008	-0.103	0.006
2593.5	-0.096	0.004	-0.107	0.004	0.0	0.2
2595.2	-0.098	0.004	-0.097	0.007
2596.9	-0.105	0.007	-0.107	0.015
2602.0	-0.066	0.010	-0.106	0.012
2603.7	-0.084	0.003	-0.102	0.009
2605.4	-0.076	0.007	-0.102	0.004
2607.1	-0.065	0.005	-0.102	0.004
2608.8	-0.067	0.015	-0.096	0.004
2610.5	-0.073	0.005	-0.089	0.007	0.0	0.2
2612.2	-0.077	0.003	-0.087	0.007	0.0	0.2
2613.9	-0.081	0.006	-0.087	0.007
2615.6	-0.068	0.007	-0.084	0.015	0.1	0.2
2617.3	-0.072	0.007	-0.085	0.007
2629.2	-0.045	0.012	-0.079	0.013
2630.9	-0.042	0.009	-0.054	0.010
2632.6	-0.049	0.004	-0.059	0.004
2634.3	-0.050	0.004	-0.077	0.004
2636.0	-0.064	0.008	-0.063	0.005
2668.3	-0.009	0.006	-0.034	0.007
2670.0	-0.020	0.006	-0.032	0.005
2678.5	-0.006	0.004	-0.024	0.004
2680.2	-0.016	0.003	-0.011	0.003	-0.1	0.2
2681.9	-0.008	0.002	-0.008	0.002
2683.6	-0.008	0.002	-0.008	0.002	0.0	0.2
2685.3	-0.005	0.002	-0.007	0.002	0.1	0.2

Table 1—Continued

V_{LSR} (km s^{-1})	Θ_x (mas)	σ_{Θ_x} (mas)	Θ_y (mas)	σ_{Θ_y} (mas)	A ($\text{km s}^{-1} \text{ yr}^{-1}$)	σ_A ($\text{km s}^{-1} \text{ yr}^{-1}$)
2687.0	0.000	0.002	0.000	0.002
2688.7	0.000	0.002	0.001	0.002	-0.1	0.2
2690.4	0.005	0.002	0.001	0.002
2692.1	0.000	0.003	0.005	0.002	-0.1	0.2
2693.8	0.009	0.002	0.006	0.002	0.0	0.2
2695.5	0.009	0.002	0.010	0.003
2697.2	0.010	0.003	0.007	0.004	-0.1	0.2
2698.9	0.014	0.002	0.010	0.002	0.1	0.2
2700.6	0.012	0.002	0.011	0.003	0.1	0.2
2702.3	0.011	0.002	0.011	0.003	-0.1	0.2
2704.0	0.013	0.003	0.011	0.004	-0.2	0.2
2705.7	0.019	0.003	0.026	0.003
2707.4	0.022	0.004	0.028	0.010	-0.3	0.2
2709.1	0.026	0.004	0.016	0.014
2710.8	0.036	0.007	0.033	0.007	-0.4	0.2
2712.5	0.052	0.004	0.029	0.007
2714.2	0.051	0.004	0.048	0.005
2715.9	0.036	0.014	0.046	0.005
2717.6	0.044	0.011	0.048	0.005
2719.3	0.062	0.006	0.054	0.009
2721.0	0.077	0.005	0.060	0.006	0.0	0.2
2734.6	0.046	0.003	0.045	0.005
2736.3	0.040	0.006	0.042	0.012	0.2	0.2
2738.0	0.045	0.008	0.054	0.006
2739.7	0.044	0.008	0.042	0.003	-0.1	0.2
2741.4	0.050	0.004	0.051	0.004	-0.1	0.2
2743.1	0.049	0.005	0.053	0.004	-0.1	0.2
2744.8	0.053	0.003	0.048	0.006	-0.2	0.2
2746.5	0.048	0.009	0.047	0.003
2748.2	0.058	0.004	0.050	0.005	-0.4	0.2
2749.9	0.058	0.004	0.052	0.014

Table 1—Continued

V_{LSR} (km s^{-1})	Θ_x (mas)	σ_{Θ_x} (mas)	Θ_y (mas)	σ_{Θ_y} (mas)	A ($\text{km s}^{-1} \text{ yr}^{-1}$)	σ_A ($\text{km s}^{-1} \text{ yr}^{-1}$)
3234.4	-0.403	0.010	-0.406	0.010	1.6	0.2
3239.5	-0.401	0.012	-0.429	0.005	1.3	0.2
3241.2	-0.404	0.005	-0.418	0.005	1.8	0.2
3242.9	-0.393	0.004	-0.433	0.004	2.5	0.2
3244.6	-0.389	0.003	-0.430	0.003	1.1	0.2
3246.3	-0.397	0.003	-0.433	0.004	1.9	0.2
3248.0	-0.397	0.004	-0.431	0.009	1.8	0.2
3249.7	-0.405	0.004	-0.438	0.008	1.6	0.2
3251.4	-0.405	0.003	-0.439	0.005	1.2	0.2
3253.1	-0.401	0.004	-0.437	0.005	1.0	0.2
3254.8	-0.413	0.007	-0.414	0.009	1.6	0.2
3256.5	-0.422	0.006	-0.442	0.011	0.9	0.2
3258.2	-0.411	0.004	-0.443	0.004	1.1	0.2
3259.9	-0.407	0.003	-0.442	0.008	1.5	0.2
3261.6	-0.406	0.004	-0.445	0.005	1.8	0.2
3263.3	-0.403	0.003	-0.463	0.015	1.9	0.2
3266.7	-0.401	0.009	-0.454	0.009	1.7	0.2
3268.4	-0.412	0.011	-0.484	0.007	1.9	0.2
3270.1	-0.402	0.006	-0.470	0.015	2.1	0.2
3271.8	-0.403	0.006	-0.478	0.006	1.9	0.2
3273.5	-0.404	0.006	-0.477	0.006	4.2	0.2
3287.1	-0.410	0.017	-0.482	0.008	2.5	0.8
3288.8	-0.406	0.004	-0.474	0.004	6.6	0.8
3290.5	-0.404	0.005	-0.506	0.005	6.1	0.8
3292.2	-0.409	0.003	-0.485	0.009	7.3	0.8
3293.9	-0.404	0.003	-0.487	0.003	8.4	0.8
3295.6	-0.403	0.003	-0.490	0.004	7.4	0.8
3297.3	-0.403	0.002	-0.492	0.006	7.2	0.8
3299.0	-0.405	0.002	-0.489	0.003	5.9	0.8
3300.7	-0.406	0.002	-0.489	0.004	5.7	0.8
3302.4	-0.409	0.002	-0.490	0.004	4.8	0.8
3304.1	-0.406	0.002	-0.493	0.002	4.7	0.8
3305.8	-0.404	0.002	-0.495	0.005	5.0	0.8
3307.5	-0.406	0.003	-0.494	0.005	5.4	0.8
3309.2	-0.404	0.002	-0.491	0.004	4.9	0.8
3310.9	-0.411	0.003	-0.493	0.003	5.9	0.8
3312.6	-0.410	0.003	-0.499	0.004	6.0	0.8
3314.3	-0.399	0.005	-0.503	0.005	5.3	0.8
3316.0	-0.412	0.010	-0.502	0.004	5.3	0.8
3317.7	-0.405	0.019	-0.499	0.005	5.5	0.8
3319.4	-0.418	0.015	-0.518	0.028	5.9	0.8
3358.5	-0.437	0.007	-0.511	0.006	2.4	0.2

Table 1—Continued

V_{LSR} (km s^{-1})	Θ_x (mas)	σ_{Θ_x} (mas)	Θ_y (mas)	σ_{Θ_y} (mas)	A ($\text{km s}^{-1} \text{ yr}^{-1}$)	σ_A ($\text{km s}^{-1} \text{ yr}^{-1}$)
3660.7	-1.198	0.010	-1.517	0.012	0.2	0.2
3735.5	-0.977	0.005	-1.139	0.008
3737.2	-0.980	0.006	-1.133	0.004	0.1	0.2
3738.9	-0.992	0.012	-1.119	0.011
3740.6	-0.971	0.005	-1.157	0.005	0.2	0.2
3745.7	-0.965	0.014	-1.143	0.020	0.2	0.2
3747.4	-0.973	0.006	-1.123	0.009
3749.1	-0.981	0.009	-1.109	0.005	-0.1	0.2
3750.8	-0.988	0.007	-1.095	0.007
3752.5	-0.965	0.011	-1.111	0.005
3754.2	-0.968	0.015	-1.094	0.008	-0.2	0.2
3755.9	-0.940	0.008	-1.092	0.004
3757.6	-0.953	0.006	-1.092	0.005	0.0	0.2
3759.3	-0.945	0.003	-1.104	0.004
3761.0	-0.944	0.004	-1.101	0.004	0.1	0.2
3764.4	-0.944	0.014	-1.082	0.015
3808.6	-0.782	0.006	-0.833	0.006
3837.5	-0.830	0.010	-0.917	0.028
3839.2	-0.811	0.009	-0.905	0.011	0.2	0.2
3840.9	-0.814	0.010	-0.914	0.005
3842.6	-0.832	0.006	-0.916	0.007
3846.0	-0.766	0.012	-0.874	0.014
3851.1	-0.791	0.007	-0.858	0.029
3859.6	-0.760	0.004	-0.848	0.005
3861.3	-0.764	0.004	-0.866	0.004
3863.0	-0.764	0.004	-0.882	0.004
3864.7	-0.760	0.007	-0.874	0.005
3866.4	-0.761	0.009	-0.868	0.007	0.3	0.2
3868.1	-0.765	0.010	-0.870	0.004
3871.5	-0.751	0.030	-0.874	0.021
3878.3	-0.761	0.016	-0.845	0.023
3880.0	-0.758	0.004	-0.871	0.004
3881.7	-0.750	0.004	-0.863	0.003	0.5	0.2
3883.4	-0.753	0.003	-0.854	0.009
3885.1	-0.746	0.003	-0.854	0.013	0.0	0.2
3886.8	-0.750	0.007	-0.865	0.005
3890.2	-0.758	0.024	-0.849	0.017
3891.9	-0.744	0.008	-0.857	0.007
3893.6	-0.715	0.006	-0.856	0.007
3903.8	-0.738	0.007	-0.830	0.005
3905.5	-0.727	0.005	-0.838	0.011
3907.2	-0.733	0.004	-0.835	0.008
3908.9	-0.727	0.004	-0.833	0.009
3910.6	-0.720	0.003	-0.827	0.004
3912.3	-0.730	0.007	-0.824	0.007
3914.0	-0.733	0.006	-0.809	0.014

Table 2. UGC 3789 Basic H₂O Maser Model

Parameter	Priors	Posterioris	Units
H_0	...	71.6 ± 5.0	$\text{km s}^{-1} \text{Mpc}^{-1}$
V_0	...	3262 ± 1	km s^{-1}
V_p	211	211	km s^{-1}
M	...	1.11 ± 0.08	$10^7 M_\odot$
x_0	...	0.402 ± 0.001	mas
y_0	...	0.460 ± 0.001	mas
$i(r_{ref})$...	90.7 ± 0.3	deg
$\partial i / \partial r$...	-8.8 ± 1.2	deg mas^{-1}
$\partial^2 i / \partial r^2$	0	0	deg mas^{-2}
$p(r_{ref})$...	221.5 ± 0.1	deg
$\partial p / \partial r$...	-3.7 ± 0.6	deg mas^{-1}
$\partial^2 p / \partial r^2$	0	0	deg mas^{-2}
e	0	0	...
ω	0	0	deg
$\partial \omega / \partial r$	0	0	deg mas^{-1}

Note. — Parameters are as follows: Hubble constant (H_0), V_{LSR} (non-relativistic, optical definition) of central black hole (V_0), peculiar velocity with respect to Hubble flow in cosmic microwave background frame (V_p), black hole mass (M), eastward (x_0) and northward (y_0) position of black hole with respect to the reference masers ($2684 < V_{LSR} < 2693 \text{ km s}^{-1}$), disk inclination ($i(r_{ref})$) at the reference angular radius of 0.604 mas, and inclination warping (change of inclination with radius parameters $\partial i / \partial r$ and $\partial^2 i / \partial r^2$), disk position angle ($p(r_{ref})$) at the reference angular radius of 0.604 mas and position angle warping (change of position position angle with radius parameters $\partial p / \partial r$ and $\partial^2 p / \partial r^2$), gas orbital eccentricity (e) and angle of pericenter with respect to the line of sight (ω) and its derivative with angular radius ($\partial \omega / \partial r$). Priors are listed for the basic model; otherwise flat priors were used. Posterioris are for the basic model.